Thin-Walled Structures 192 (2023) 111115

Contents lists available at ScienceDirect

Thin-Walled Structures

journal homepage: www.elsevier.com/locate/tws

Full length article

Elastically anisotropic architected metamaterials with enhanced energy absorption

Huan Jiang [a], Brett A. Bednarcyk [b], Louise Le Barbenchon [c], Yanyu Chen [a,*]

[a] Department of Mechanical Engineering, University of Louisville, Louisville, KY 40292, USA
[b] NASA Glenn Research Center, Cleveland, OH 44135, USA
[c] Arts et Métiers ParisTech, CNRS, I2M Bordeaux, Esplanade des Arts et Métiers, Talence Cedex, F-33405, France

ARTICLE INFO

Keywords:
Anisotropy
Energy absorption
Metamaterial
Ellipsoidal shell
3D printing

ABSTRACT

Materials and structures featuring a combination of high stiffness, strength, and energy absorption are highly demanded. Current studies are focused on the improvement of these mechanical properties without considering their directional dependence. In practice, directional-dependent mechanical properties are crucial to structural integrity and performance, for instance, in the application of anisotropic bone scaffolds for load bearing and battery separators for ion conductivity. Recently, tunable anisotropic stiffness in mechanical metamaterials has been obtained by tailoring the microstructures using data-driven approaches. However, energy absorption behavior, which plays a critical role in the presence of large deformation, has largely been neglected. In this work, we propose a new type of elastically anisotropic architected metamaterials (AAMs) inspired by the current lithium-ion battery separator porous microstructure to acquire tunable anisotropy while exhibiting superior energy absorption. The integrated study presented herein, which combines an experimental investigation with numerical simulations, reveals that the anisotropy can be engineered across a broad range. Compared with two existing lattice and shell-based architected materials, it is shown that the energy absorption of the newly developed AAMs is increased by 120% and 13%. The findings in this work provide a new strategy to expand the existing metamaterial design space, with the potential to enable innovative solutions for applications where directional-dependent stiffness and energy absorption are needed.

1. Introduction

Materials and structures featuring a combination of stiffness, strength, and energy absorption are needed for applications where extreme loading conditions occur. Conventional designed and manufactured structures have reached a bottleneck and failed to meet the growing requirements in some such circumstances. The advancement of additive manufacturing has provided a new route to produce engineered materials with highly tailored material architectures. These architected metamaterials have demonstrated unprecedented mechanical properties. For example, architected materials with lattice topology manufactured by projection micro-stereolithography show nearly linear scaling between stiffness and density [1] and overcome the impediment of degradation in mechanical properties as density decreases. Plate-nanolattices fabricated via two-photo lithography are reported to reach the Hashin–Shtrikman and Suquet upper bounds, demonstrating unparalleled specific strength that surpasses that of bulk diamonds [2]. Shellular structures [3] have also been designed with superior strengths that are close to the theoretical limits. Furthermore, enlightened by the unique behavior of a bistable elastic tilt-beam, a multi-stable architected material has been proposed, enabling the elastic strain energy to be efficiently trapped and offering a new strategy to design structures with enhanced energy absorption [4]. In addition, multi-stiffness metamaterials featuring with zero Poisson's ratio was designed, the tunable deformation behavior enables them to be good candidate for energy absorbers [5,6]. Novel auxetic metamaterials have demonstrated excellent energy absorption while maintaining auxetic characteristics [7,8]. By leveraging the synergistic interaction between the structural energy trapping provided by a tilted plate and the inherent material dissipation associated with liquid crystal elastomers, novel rate-dependent energy absorption behavior has been observed [9].

Apart from the abovementioned rationally designed architected materials, nature has provided a rich source of inspiration for fresh designs. For example, a sea sponge-inspired lattice design was found to provide a superior mechanism for withstanding loads before the onset of buckling for a wide range of loading conditions, and the corresponding optimization efforts showed that the architecture of the sponge skeleton is nearly identical to the optimal lattice design, offering the highest critical stress under uniaxial compression [10]. Inspired by the dactyl club from the mantis shrimp, a nanoparticle-coated co-continuous composite has been shown to significantly improve the

* Corresponding author.
E-mail address: yanyu.chen@louisville.edu (Y. Chen).

https://doi.org/10.1016/j.tws.2023.111115
Received 1 June 2023; Received in revised form 11 August 2023; Accepted 12 August 2023
Available online xxxx
0263-8231/

energy dissipation behavior by pulverizing the primary particles into smaller fractured secondary grains when a high-strain-rate impact occurs [11]. Utilization of biologically inspired composites can not only reduce the energy formation of the coating particles but also set a low barrier to fracture, which enables large, localized energy absorption. Other nature-inspired structures also provide valuable design concepts to achieve outstanding mechanical properties [12,13]. Although the architected materials from both rational design and bio-inspired design have achieved exceptional mechanical performance, the aforementioned works are largely focused on isotropic materials, neglecting the potential benefits of directional dependent mechanical properties.

Anisotropy, which refers to material behavior in which reactions are different to stresses applied in different directions, is ubiquitous in nature and engineering materials. One major application of the anisotropic feature is to reinforce the mechanical properties along prime directions, given that the applied strain/stress conditions are rarely equiaxed in practice [14]. For example, the multiscale hierarchical structure of wood, consisting of aligned cellulose nanofibrils and a complex porous microstructure in the growing direction, has been extensively studied [15]. Such hierarchical anisotropic structures, and the organization of the organic phases at the nanoscale, offer a unique combination of exceptional mechanical properties to resist external load and biological functions such as the absorption of nutrients [16]. Cortical bone is characterized by unidirectional mineralized collagen fibrils in a non-collagenous matrix within each lamella of osteons, which are further assembled along the bone's length direction [14]. These microstructural features determine the directional-dependent mechanical properties of cortical bone. Essentially, the specific topology is optimized for the long-term complex mechanical environment, which demands optimal strength and load transmission in the main load-bearing direction, while simultaneously keeping the bone mass as low as possible [17]. In lithium-ion batteries, the crucial component of the separator is characterized by a strong anisotropy [18–22] due to the oriented reinforcement fibers [23]. A four-fold difference in the stiffness, and a nearly ten-fold difference in failure stress, have been observed in the separator between the machine direction (MD) and transverse direction (TD) [23]. While the current commercial separators are manufactured with stochastic microstructures, separators with uniform morphologies and tight pore size distributions are highly desirable [24].

The development of architected materials with anisotropy is still in its infancy, with a few studies reported in the literature. For example, inspired by the natural self-assembly process via spinodal decomposition, tunable elastic anisotropy has been demonstrated in a new class of nano-labyrinthine materials. These employ self-assembled double-curvature shell architectures and strong nanoscale effects [25]. Furthermore, by leveraging a robust machine learning technique to train the spinodal topologies, tailored directional-dependent stiffness was obtained [26]. Recently, by combining the tunable anisotropy of spinodal architected materials with multiscale topology optimization, an optimized macroscale structure, with free-varying orientation and porosity, has been fabricated that can be used in supporting directional-dependent mechanical demands [27]. As an attempt to design compatible bone implants, four types of lattice structures were investigated systematically, and the relationship between the anisotropy coefficient and geometric parameters was mapped [17]. Representative topologies of six cellular structures were studied, and it was shown that only this anisotropic material can achieve stiffnesses in excess of the Hashin–Shtrikman upper bound [28]. Interestingly, this work also revealed that the anisotropy of the combination of cubic and octet foam can be tailored by adjusting the ratio of the wall thicknesses. Although the aforementioned studies provide an avenue to achieve tunable anisotropy, these works are focused on the directional dependent elastic properties, i.e., stiffness. The studies of mechanical performance of anisotropic materials under large deformations, such as those associated with energy absorption, are quite limited.

In this work, we develop a simple new type of anisotropic architected metamaterials (AAMs) by taking inspiration from the shape of the voids within the lithium-ion battery separators, as shown in **Figure S1**. We use the ellipsoidal shell to represent the lamellae and beam connectors to denote the fibers. It should be pointed out that this design is enlightened by the anisotropy of commercial battery separators, and uniform morphological separator design (compared to the stochastic feature of commercial separators) as required for batteries [29] can be obtained by this AAM. However, how the different anisotropy will affect the separators in battery applications is not the scope of this study. This AAM consists of ellipsoidal shells and beams. We have previously shown that this type of metamaterial exhibits enhanced energy absorption [29] and remarkable vibration mitigation properties [30,31]. Here, we study the anisotropic features and mechanical performance of AAMs under large deformation by altering the ratio of the major axis and minor axis of ellipsoidal shells. We first benchmark the mechanical performance of AAMs under large deformation, followed by the finite element analysis (FEA) of the directional dependent elastic stiffness by applying periodic boundary conditions (PBC), along with experimental validation. Finally, we show that the developed AAMs display superior energy absorption behavior in comparison to existing architected materials.

2. Materials and methods

2.1. Anisotropic architected metamaterial design

Different from many of the currently studied mechanical metamaterials that are characterized by cubic symmetry (Fig. 1**(a)**), we designed an ellipsoidal mechanical metamaterial with tetragonal symmetry, as shown in Fig. 1**(b), (c), (d)**. The different symmetrical systems are shown in **Figure S2** and the mechanical properties corresponding to different symmetrical systems are detailed in the **SI**. The Representative Volume Element (RVE) is shown in Fig. 1**(e)**. It consists of a perforated shell component (Fig. 1**(e)**) and a binder component (Fig. 1**(e)**). The shell component is designed by specifying the major axis a and minor axis b of an ellipse and then rotating about the major axis (Fig. 1**(e)**). r is the radius of the perforation, and t denotes the thickness of the shell. The shell perforation is mainly for the 3D printing purposes, as the closed shell will contain extra material powder inside which is unable to remove. All the perforations were drilled along the diagonal direction in RVE. The binder component, which consists of the same base material as the shell, is characterized by the fillet radius R, cross-section diameter d, and mid-axis length s. The procedure of creating the binder is that: (1) we draw a curved line with radius of R, its distance to main axis is set to d; (2) rotate this line 360°to get the surface; (3) use the boolean difference command in Rhino software to create the binder structure. In the designs considered, r/a=1/6, t/a=1/12, s/a=1/12, d/a=1/4, and R/a=5/6. For all of the AAM designs, the major axis a is fixed to $a = 25$ mm, and the minor axis b is varied to obtain different configurations. The as-manufactured AAMs consist of 3 × 3 × 3 RVEs. Fig. 1**(f)–(i)** show the 3D printed samples corresponding to the designs with $a/b = 1$, $a/b = 1.2$, $a/b = 1.5$, and $a/b = 2$, respectively. It should be noted that because the shell thickness in this design is kept the same, the relative densities of four different configurations in Fig. 1**(a)** are different. The relative densities are 13.25%, 12.11%, 11.02%, and 10.14%, respectively. The results obtained from experiments and simulations will be normalized by relative density in order to compare their mechanical performance legitimately, as will be mentioned later in the discussion.

2.2. Fabrication

The AAMs were fabricated by additive manufacturing using an HP jet fusion 580 printer (HP Inc., USA). The HP 580 printer is renowned for its exceptional multi-agent and multi-pass printing capabilities. The

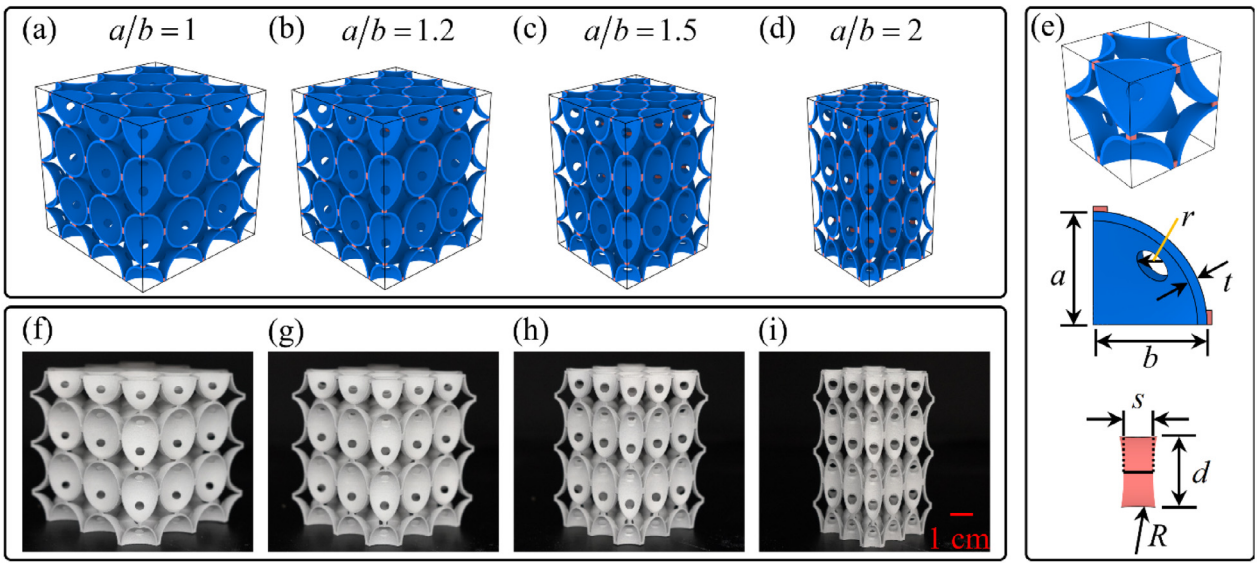

Fig. 1. AAMs with different designs. (a)–(d) AAMs with a/b = 1, a/b = 1.2, a/b = 1.5, and a/b = 2, respectively. (e) Representative volume element (RVE), one-eighth model of the RVE and the binder geometry. Here, a/b = 1, r/a=1/6, t/a=1/12, s/a=1/12, d/a=1/4, and R/a=5/6. (f)–(i) 3D printed samples for a/b = 1, a/b = 1.2, a/b = 1.5, and a/b = 2, respectively.

multi-jet fusion process is a specific additive manufacturing technique that is utilized for fabricating parts and prototypes. It involves the use of a printer equipped with multiple inkjet arrays to deposit and fuse various agents onto a powdered material. This 3D printing technique involves following steps: (1) material preparation; (2) agent deposition; the agents include fusing agents, detailing agents, and coloring agents; (3) Thermal fusing; after the agent deposition, the agents are exposed to thermal energy which will melt and fuse the particles of the powered material together; (4) layering and repetition; once the first layer has been fused, new layer is spread. This layer-by-layer approach is repeated until the entire part is built. By utilizing multiple inkjet arrays and carefully controlling the deposition of fusing, detailing, and coloring agents, the multi-jet fusion process enables the production of complex and customized parts with high-resolution finishes. The fused layers lock together at the molecular level, resulting in strong and durable final products. In this study, we utilized Nylon-12 as the base material. Nylon-12 is a widely employed material in injection molding and has gained popularity as a common base material in additive manufacturing. It possesses desirable characteristics, such as excellent processability, high mechanical properties at moderate temperatures [32], and relatively low costs. It should be pointed out that despite the advantages of the printer, we cannot manufacture the AAMs with very low relative density (below 10%) because of the limitation of resolution and difficulty of cleaning the samples.

2.3. Mechanical testing

The quasi-static compression tests on the AAMs were carried out to investigate the elastic stiffness and mechanical behavior under large deformations. All the AAM samples were uniaxially compressed using an Instron universal testing machine (5569 A, Instron Corp., USA) with a 50 kN load-cell at a constant strain rate of $\sim 10^{-4}$ s^{-1} (3.75 mm/min). The samples were compressed to maximum strain of 70%, i.e., 52.5 mm. The stiffness and strength of the AAM samples were extracted from the experimental stress–strain curve [33]. The energy absorption of the tested architected materials was determined by calculating the area under the stress–strain curve [34]. In the repeated experiment, four tests were conducted to ensure repeatability. Besides, we installed the 2D Digital Image Correlation (DIC) (GOM, Germany) to capture the deformation pattern. The morphologies and the failure modes for the samples captured by DIC were used for the following analysis and discussion. Additionally, three fully dense dumbbell-shaped samples were tested to calibrate the Nylon-12 constitutive model for the finite element simulations.

2.4. Finite element simulations

2.4.1. Finite element simulation setup

Finite element (FE) simulations were performed to analyze the anisotropic behavior of AAMs and to gain additional insights into the mechanisms of deformation. The simulations utilized the Abaqus/Explicit (Providence, RI, USA) solver. The 3 × 3 × 3 models were simulated to investigate the mechanical behavior under large deformation. The FE simulation setup is displayed in **Figure S3 (a)–(b)**. The rigid bottom plate was fixed translationally as well as rotationally. The rigid top plate was subjected to downward displacement, i.e., 52.5 mm. In the simulations, an elastic-perfectly plastic constitutive model, calibrated with experimental data on fully dense Nylon-12, was employed (**Figure S3 (d)**). Note that the employed Young's modulus for Nylon-12 is E = 1400 MPa, the Poisson's ratio is ν = 0.3, and the yield stress is 38 MPa [29]. To simulate the contact behavior, general self-contact with a friction coefficient of 0.25 for tangential motion and hard contact for the normal direction were defined [35,36]. All the architected materials simulated in this work were meshed with ~300,000 C3D8 elements by Hypermesh (Altair Engineering Inc, USA). The converged simulation results are depicted in **Figure S3 (e)–(f)**. To satisfy the quasi-static simulation requirement, dynamic effects are kept negligible by controlling the ratio of kinetic energy to internal energy below 5% [29]. Furthermore, to understand the elastic response of AAMs, the RVE models were simulated to study the anisotropic behavior by applying periodic boundary conditions (PBCs), wherein the linear elastic model is applied since only small deformation is considered.

2.4.2. Periodic boundary conditions

As discussed before, the anisotropic metamaterials can be considered as a periodic array of RVEs. Therefore, periodic boundary conditions can be applied in order to reduce the computational load while maintaining high accuracy. As pointed out in the Ref. [37], the deformation between adjacent RVEs should be compatible, and there is no distance between them as well as they do not overlap. The periodic boundary conditions can be expressed as follows [38]:

$$u_i\left(x_1, x_2, x_3\right) = \bar{\varepsilon}_{ik} x_k + u_i^*\left(x_1, x_2, x_3\right) \quad (1)$$

where $\bar{\varepsilon}_{ik}$ is the average strain and $u_i^*\left(x_1, x_2, x_3\right)$ is a periodic function from one RVE to the next, which is essentially unknown and dependent on the general loading.

Because of the periodicity of RVEs, two types of continuity are required in boundary conditions: first, the displacements need to be continuous; second, the traction distribution in the opposite boundaries should be the same. Therefore, the displacement for the boundary surfaces of parallel pairs should follow the equation below [37]:

$$u_i^{j+} = \bar{\varepsilon}_{ik} x_k^{j+} + u_i^* \tag{2}$$

$$u_i^{j-} = \bar{\varepsilon}_{ik} x_k^{j-} + u_i^* \tag{3}$$

where the $j+$, $j-$ superscript means the jth pair of opposite surfaces in RVE.

As $u_i^*\left(x_1, x_2, x_3\right)$ is unknown, combining Eqs. (2) and (3), the following equation can be obtained:

$$u_i^{j+} - u_i^{j-} = \bar{\varepsilon}_{ik}\left(x_k^{j+} - x_k^{j-}\right) = \bar{\varepsilon}_{ik}\Delta x_k^j \tag{4}$$

The above equation can be applied in ABAQUS by defining MPC constraints through python script.

On the other hand, the traction continuity requirement for opposite parallel surfaces can be expressed as [37]

$$\sigma_n^{j+} - \sigma_n^{j-} = 0 \tag{5}$$

$$\tau_{nt}^{j+} - \tau_{nt}^{j-} = 0 \tag{6}$$

where σ_n and τ_{nt} denote the normal and shear stress in opposing parallel surfaces.

However, it has been proven in Ref. [39] that in a displacement-based finite element analysis, Eq. (4) guarantees the uniqueness of solution; Eqs. (5) and (6) will automatically be satisfied.

3. Results and discussion

3.1. Effect of ratio of major axis to minor axis

3.1.1. Mechanical performance under large deformation

To understand the mechanical behavior of the AAMs under large deformations, uniaxial compression tests have been performed. For clarity, all the experimental and simulated results in this section are normalized with respect to the relative density of each AAM. The experimental normalized nominal stress–strain curves for AAMs with $a/b = 1$, $a/b = 1.2$, $a/b = 1.5$, $a/b = 2$ are shown in Fig. 2**(a)**. It can be observed that the ratio a/b significantly affects the mechanical performance of AAMs. Specifically, as the ratio of a/b increases, the stress also rises, especially before the yield strength. However, the stress–strain curve is characterized by an increasing peak–valley feature. This indicates that significant buckling occurs as the ratio of a/b becomes larger, as will be evidenced by the deformation images in the following. It is interesting to find that the AAMs with $a/b = 2$ exhibits significant negative stiffness behavior; this unique behavior is attributed to the occurrence of shell buckling. This phenomenon has been harnessed to create efficient energy absorbers [5,40]. Fig. 2**(b)** displays the experimental and FE simulation results for the stress–strain curve of AAM with $a/b = 1$ and $a/b = 2$. In our simulation, we did not consider the fracture or failure. Therefore, notable difference between experiment and simulation is observed in Fig. 2**(b)**. However, the FE simulation does a good job of capturing the significant qualitative features observed in the experimental stress–strain responses until densification. Fig. 2**(c)** and **(d)** show the experimental deformation pattern for different applied strain levels. At strain of $\varepsilon = 0.12$, the AAM with $a/b = 1$ exhibits monolithic deformation behavior, and no significant localized deformation is observed. By contrast, the AAM with $a/b = 2$ displays notable localized buckling at the top layer, which corresponds to the first peak–valley section on the stress–strain curve. As the strain increases, the AAM with $a/b = 1$ shows the same deformation pattern with uniform deformation of each layer until densification. This explains the smooth appearance of stress–strain curve in Fig. 2**(a)**. On the other hand, the AAM with $a/b = 2$ exhibits a layer-by-layer buckling behavior at different strain stages which corresponds to the different peak–valley sections on the stress–strain curve in Fig. 2**(a)**. The layer-by-layer deformation pattern has been previously determined to contribute to energy absorption performance by preventing an early catastrophic failure mode [41].

To gain further insights about the deformation mechanisms of the AAMs, von Mises stress contour plots from the finite element simulations are shown in Fig. 2**(e)** and Fig. 2**(f)**. At an applied strain of $\varepsilon = 0.12$, the stresses for the AAM with $a/b = 1$ are largely concentrated on the binder regions, which, recall, are present to hold the ellipsoidal shells together (see Fig. 1). It can be observed that the stresses (and deformations) distributed on the spherical shells are quantitatively quite similar for the different layers. This agrees with the experimental observation of monolithic deformation behavior at this stage for the AAM with $a/b = 1$. However, the stresses for the AAM with $a/b = 2$ are mainly concentrated on the top layer, as shown in Fig. 2**(f)**. This helps explain the first peak–valley section in Fig. 2**(a)** and is consistent with the experimental observations in Fig. 2**(d)**. As the strain rises, similar deformation mechanisms compared to strain of $\varepsilon = 0.12$ are revealed, i.e., global buckling mode for the AAM with $a/b = 1$ and localized layer-by-layer buckling mode for the AAM with $a/b = 2$. The deformation mechanisms shown in these finite element simulations further explain the experimental observations in Fig. 2**(c)** and **(d)**.

The normalized stiffness, yield strength, and energy absorption are plotted against the AAMs with $a/b = 1$, $a/b = 1.2$, $a/b = 1.5$, $a/b = 2$ in Fig. 3, respectively. The energy absorption is defined by the area under the stress strain curve. As the ratio of a/b increases, the stiffness, yield strength, and energy absorption exhibit an increasing trend. Specifically, a four times increase in stiffness and a three times increase in yield strength has been observed as the ratio of a/b increases from 1 to 2. However, the increase in energy absorption is not as significant as stiffness and yield strength, and it reaches a threshold when $a/b = 1.5$. This is mainly because of the peak–valley characteristics in the stress–strain curve (due to the localized layer-by-layer buckling behavior) for $a/b = 2$ compared to the smoother monolithic deformation patterns observed for lower a/b values.

3.1.2. Scaling law and anisotropy

To achieve high effective strength in metamaterial, local stretching-dominated behavior is usually desirable. Conventionally, cellular foam structures tend to exhibit local bending-dominated deformation modes [42–44]. Recently, the Triply Periodic Minimal Surface (TPMS) based foam topology has demonstrated local stretching-dominated behavior [45,46]. Interestingly, TPMS-based Schwarz-P soft pneumatic actuator was studied to exhibit anisotropic behavior when pressurized [47]. However, the limitation of TPMS-based foam is the limited tunability of its mechanical performance due to the lack of enough design parameters. Here, we show that by altering the ratio of a/b in AAMs, the deformation mode can be transformed from bending-dominated to stretching-dominated. A single RVE (Fig. 4**(a)**) finite element model with periodic boundary conditions (as described in Section 2.4) was developed to predict the initial linear elastic properties of the AAMs. The scaling law of relative stiffness E/E_s versus relative density ρ/ρ_s, as well as the projection of stiffness varied between the [100] and [001] directions of the RVE, are plotted in Fig. 4**(b)** (where E_s and ρ_s are the Young's modulus and density of the base Nylon-12 material, respectively). Note that the relative density of each AAM configuration was altered by changing the shell thickness, t. The results show that the relative stiffness, E/E_s, increases in direct proportion to the rising relative density, ρ/ρ_s, regardless of the different AAM architectures. Meanwhile, as the ratio of a/b increases, the power index of the scaling law decreases. This decrease in the power index indicates a more stretching-dominated behavior as the relative stiffness is less affected by simply increasing the shell thickness, which is also closer to

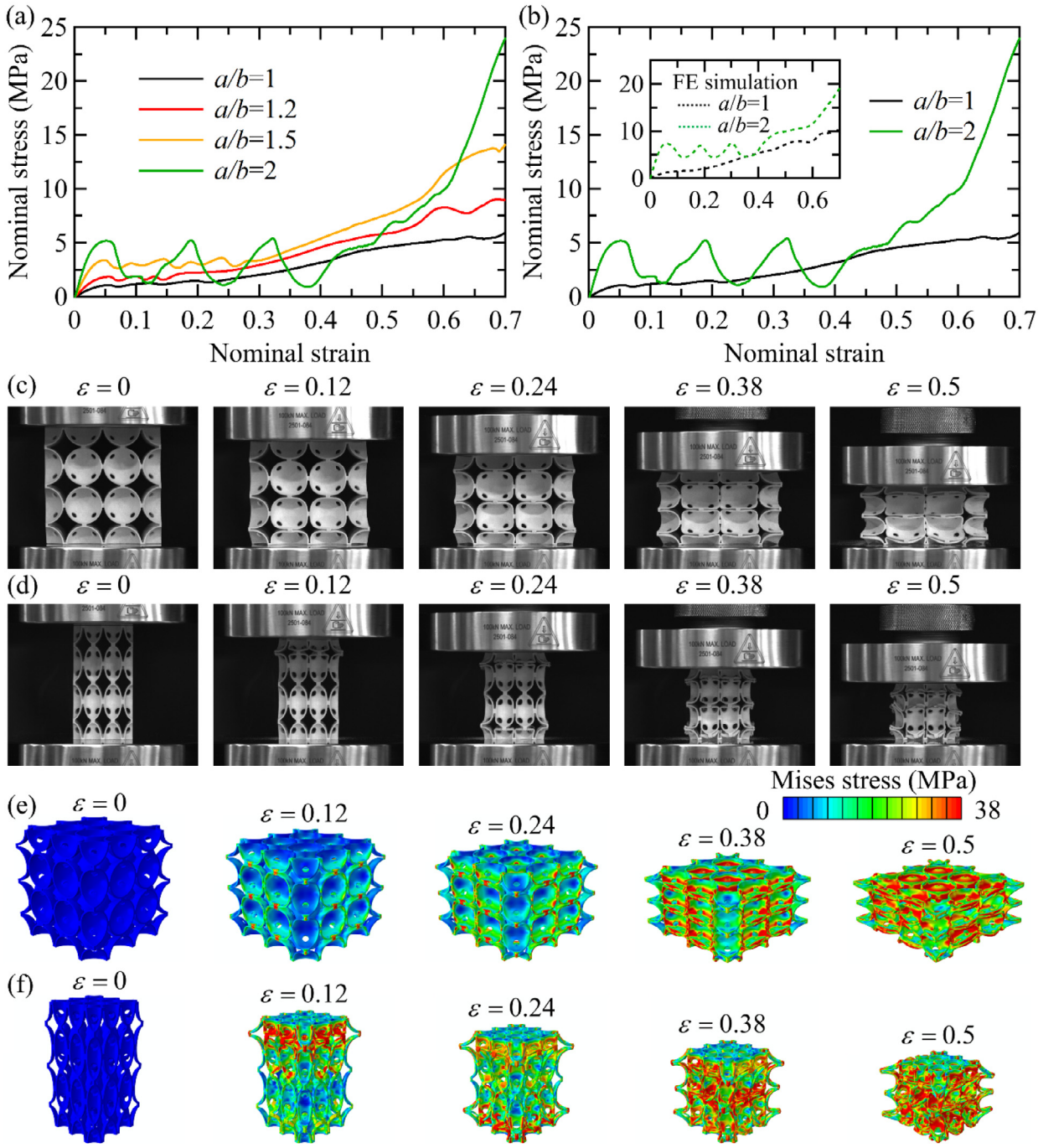

Fig. 2. Experiment and simulation results for AAMs. (a) Normalized nominal stress–strain relation for AAMs with a/b = 1, a/b = 1.2, a/b = 1.5, and a/b = 2, respectively. (b) Experimental and simulated normalized nominal stress–strain relation for $a/b = 1$ and $a/b = 2$, inset is FE simulation results. (c) Deformation patterns for $a/b = 1$ and $a/b = 2$. (d) Von-Mises stress contour plots for $a/b = 1$ and $a/b = 2$.

the theoretical limit. The power index evolution affected by geometric parameters was explicitly observed in a similar study [48], wherein the strut angle of BCC lattices was shown to alter the deformation mechanism. The design strategy studied here could expand the design space to achieve tunable mechanical behavior.

Many current metamaterial design studies focus on materials in which the three orthogonal directions [100], [010] and [001] exhibit the same modulus [28,49,50]. In contrast, the AAMs described herein exhibit significant anisotropy for three principal orthogonal directions. For instance, in the E_x vs. E_z plots in Fig. 4**(c)**, which examine the effective stiffness in the x-z plane, the AAM with $a/b = 1$ shows a square-like shape with equal stiffness along [100] and [001] directions. In contrast, the AAM with $a/b = 2$ exhibits two elliptical lobes, and the ratio of stiffness along [001] direction to [100] direction is 17. Comparatively, the ratio of the stiffness for stochastic lattice and rhombic dodecahedron lattice along [001] to [100] direction has been shown to vary from 1.3 to 5 [51], which is significantly smaller than the difference reported in our study. Additionally, a qualitative agreement between the experimentally measured and numerically simulated stiffness along different directions is observed (Fig. 4 **(c)**). The more detailed anisotropic behavior of AAM is described in Fig. 5 and will be discussed in the following.

The mechanical anisotropy of the AAMs is represented by the elastic surfaces, which convey the orientation-dependent sample stiffness

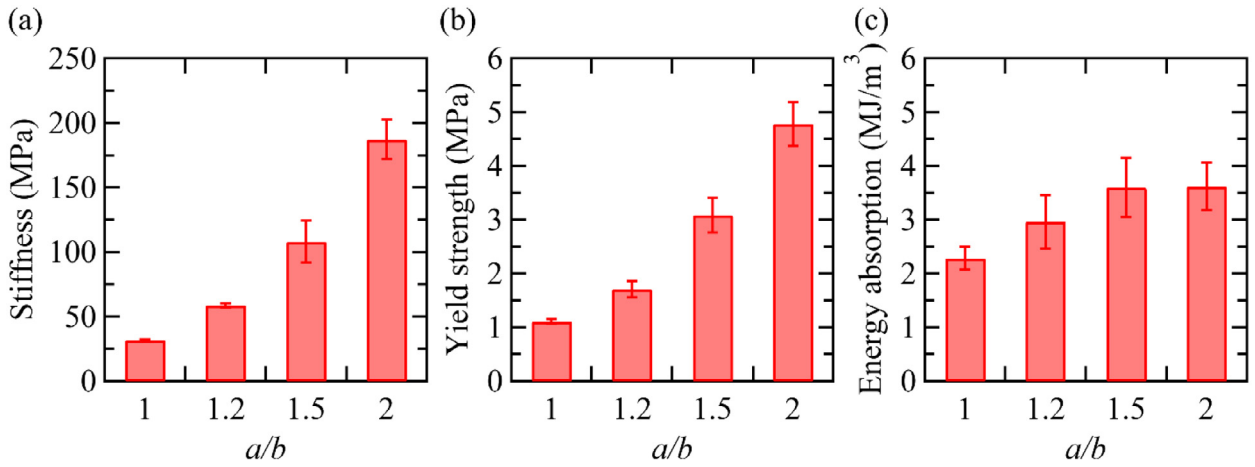

Fig. 3. Effect of a/b on the mechanical performance of AAMs. (a) Effective stiffness as a function of a/b. (b) Yield strength as a function of a/b. (c) Energy absorption as a function of a/b.

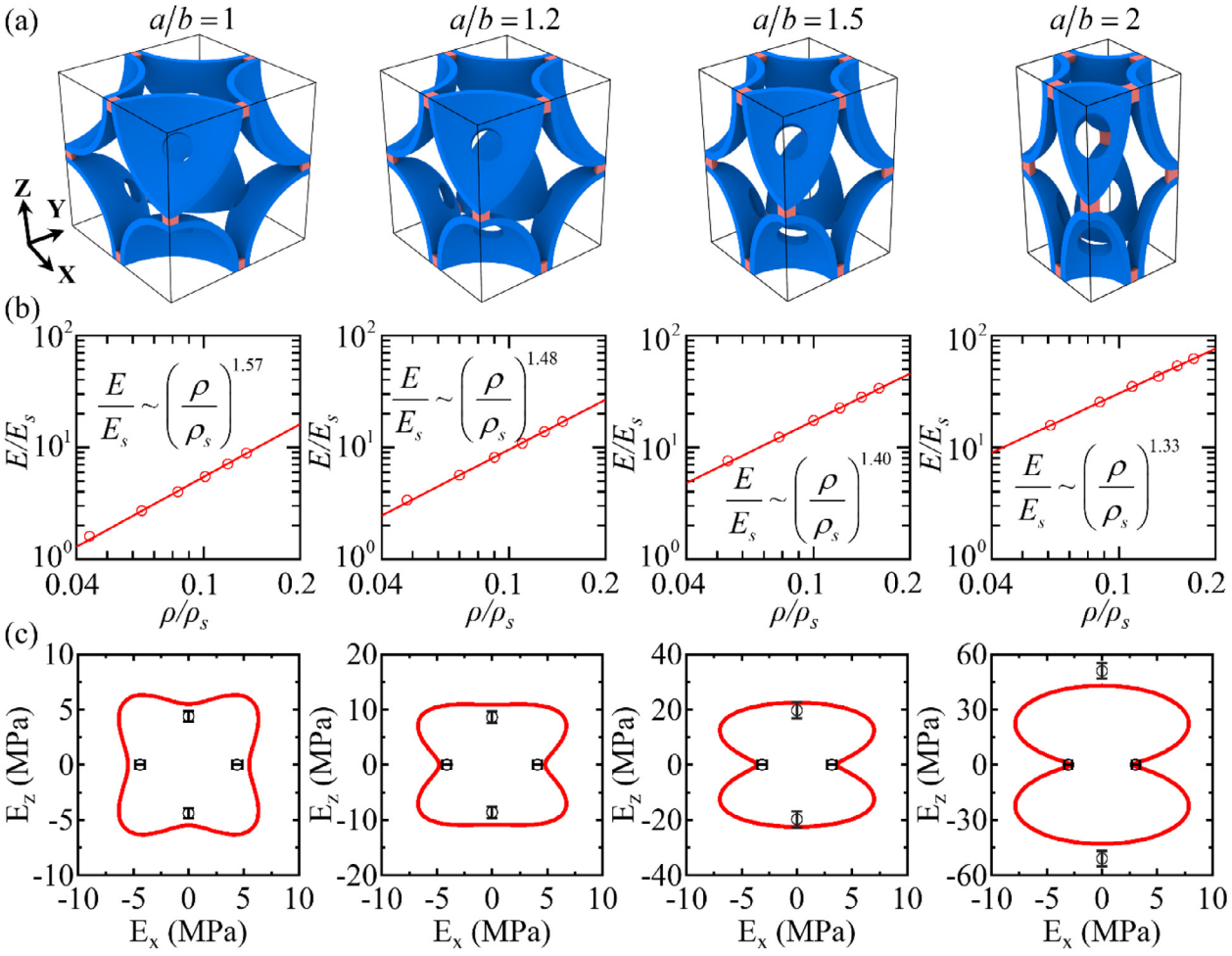

Fig. 4. Effect of a/b on the elastic response of AAMs. (a)–(c) Geometrical model, relative stiffness as a function of relative density, and 2D spatial representations of specific effective Young's modulus surfaces of AAMs for $a/b = 1$, $a/b = 1.2$, $a/b = 1.5$, and $a/b = 2$, respectively.

(i.e., Young's modulus E as a stiffness measure under uniaxial loading), Poisson's ratio, and shear modulus calculated using linear elastic finite element models. We implemented a homogenization scheme with periodic boundary conditions to calculate the elastic properties in all directions [52]. Fig. 5 **(a)** shows the spatial distribution of effective Young's modulus normalized with the maximum Young's modulus. For the AAM with $a/b = 1$, the prime direction with maximum Young's modulus is [111] direction while the [100], [010], and [001] directions show the minimum Young's modulus value. As we increase the ratio of a/b, the prime direction shifts from the [111] to the [1] direction. The [100] and [010] directions remain those with minimum Young's modulus. This demonstrates that altering the ratio of a/b allows for prescribing substantial elastic anisotropy and provides a mechanism to design the elastic response along chosen directions in a single

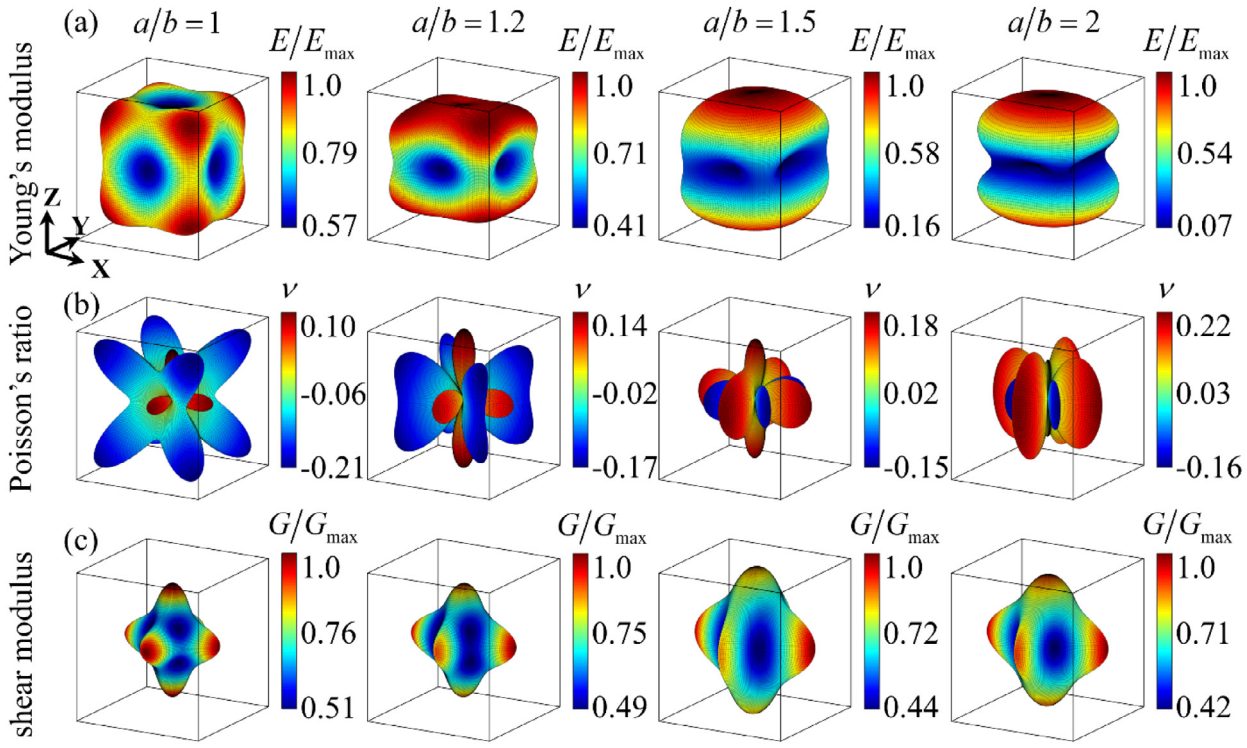

Fig. 5. Spatial distribution of effective Young's modulus, Poisson's ratio and shear modulus for AAMs with $a/b = 1$, $a/b = 1.2$, $a/b = 1.5$, and $a/b = 2$. (a) effective Young's modulus normalized with maximum Young's modulus. (b) effective Poisson's ratio. (c) effective shear modulus normalized with maximum shear modulus.

architecture. The spatial distribution of the effective Poisson's ratio is shown in Fig. 5 (b). It is interesting to find that the [111] direction of the AAM with $a/b = 1$ shows significant negative Poisson's ratio. As the ratio of a/b increases, the negative Poisson's ratio extremum shifts gradually from the [111] direction to the [110] direction, and the negative Poisson's ratio becomes less and less significant. The regions associated with negative Poisson's ratio shrink continuously at the same time. Fig. 5**(c)** exhibits the spatial distribution of the effective shear modulus. All four architectures display a gyroscopic distribution of shear modulus. Specifically, the minimum value of shear modulus lies in the [111] direction while the maximum is along the [100], [010], and [001] directions for the AAM with $a/b = 1$. Similar to the Poisson's ratio, the minimum value of shear modulus shifts from the [111] direction to the [110] direction as the ratio of a/b enlarges.

3.2. Comparison of AAM with existing architected materials

In order to further compare the mechanical performance of AAM with the existing architected materials, we designed example SC (Simple Cubic)-lattice and SC-TPMS as shown in Fig. 6**(a)**. Here, the AAM was designed based on major–minor axis ratio $a/b = 2$. In this section, we kept the same lattice constant and relative density for the three designs. The relative densities of these designs were determined by the ratio of the volume of architected materials to the volume of bounding box; the volume of architected materials was obtained by measuring it directly in Rhino software. Keep in mind that we choose SC-TPMS as the base material for our comparison is because our design of AAM is SC symmetric. The symmetric type could significantly affect the energy absorption behavior [53]. Here, we conducted experiments and FE simulations to study the mechanical behavior of the three designs under large deformation. The compressive stress–strain curves for the three architected materials are shown in Fig. 6**(b)**. The SC-lattice displays compelling mechanical behavior compared to SC-TPMS and AAM before the yield strength because of the strong stretch-dominated behavior of SC-lattice when loading in the [1] direction [54]. However, after the peak strength, the stresses drop significantly and maintain in a low level. The SC-TPMS shows a lower yield strength than SC-lattice but larger than AAM. Stress also drops notably after the peak strength. The AAM, on the other hand, exhibits a similar deformation pattern of peak–valley feature as discussed before (see Section 3.1). The deformation images of SC-lattice, SC-TPMS and AAM are shown in Fig. 6**(d)**, **(e)**, and **(f)**. At an applied strain of $\varepsilon = 0.07$, the top front of the SC-lattice failed catastrophically, corresponding to the abrupt drop of stress in Fig. 6**(b)**. At this stage, the SC-TPMS and AAM show continuous deformation, as evidenced by the smooth rising of stress in Fig. 6**(b)**. At an applied strain of $\varepsilon = 0.12$, the failure of SC-lattice expands to the backside of the middle layer causing global instability, which is verified by the further drop of stress to the minimum value during the experiment (Fig. 6**(b)**). In contrast, the SC-TPMS displays observable buckling of all the cells, indicating the steady rising of stress (Fig. 6**(b)**). On the other hand, the AAM exhibits a layer-by-layer deformation pattern, with significant buckling behavior of the bottom layer. This corresponds to the first peak–valley section on the stress–strain curve in Fig. 6**(b)**. As the strain rises, the SC-lattice shows further failure until the total collapse of top layer. The SC-TPMS exhibits failure of the top layer at an applied strain of 0.2, as evidenced by the notable stress drop in Fig. 6**(a)**. The middle layer of SC-TPMS also fails in a brittle manner at an applied strain of 0.5, leading to minimal. Meanwhile, the AAM is characterized by a layer-by-layer deformation pattern until densification, indicating a stable mechanical behavior at large deformation with a great deal of energy absorption.

As noted in the above experimental analysis, the failure of the SC-lattice and SC-TPMS dominate their mechanical performance at large deformation. In order to further demonstrate the superior design of AAM and eliminate the effects of inadequate ductile property of nylon material. We numerically simulated the three architectures for large deformation behavior with no failure incorporated. The stress–strain curves for the SC-lattice, SC-TPMS, and AAM are shown in Fig. 6**(c)**. It shows very similar mechanical behavior before the failure when compared to the experimental results. The stiffness, yield strength, and energy absorption of the three designs from experimental and numerical results are displayed in Fig. 7. As shown in Fig. 7 **(a)** and **(b)**,

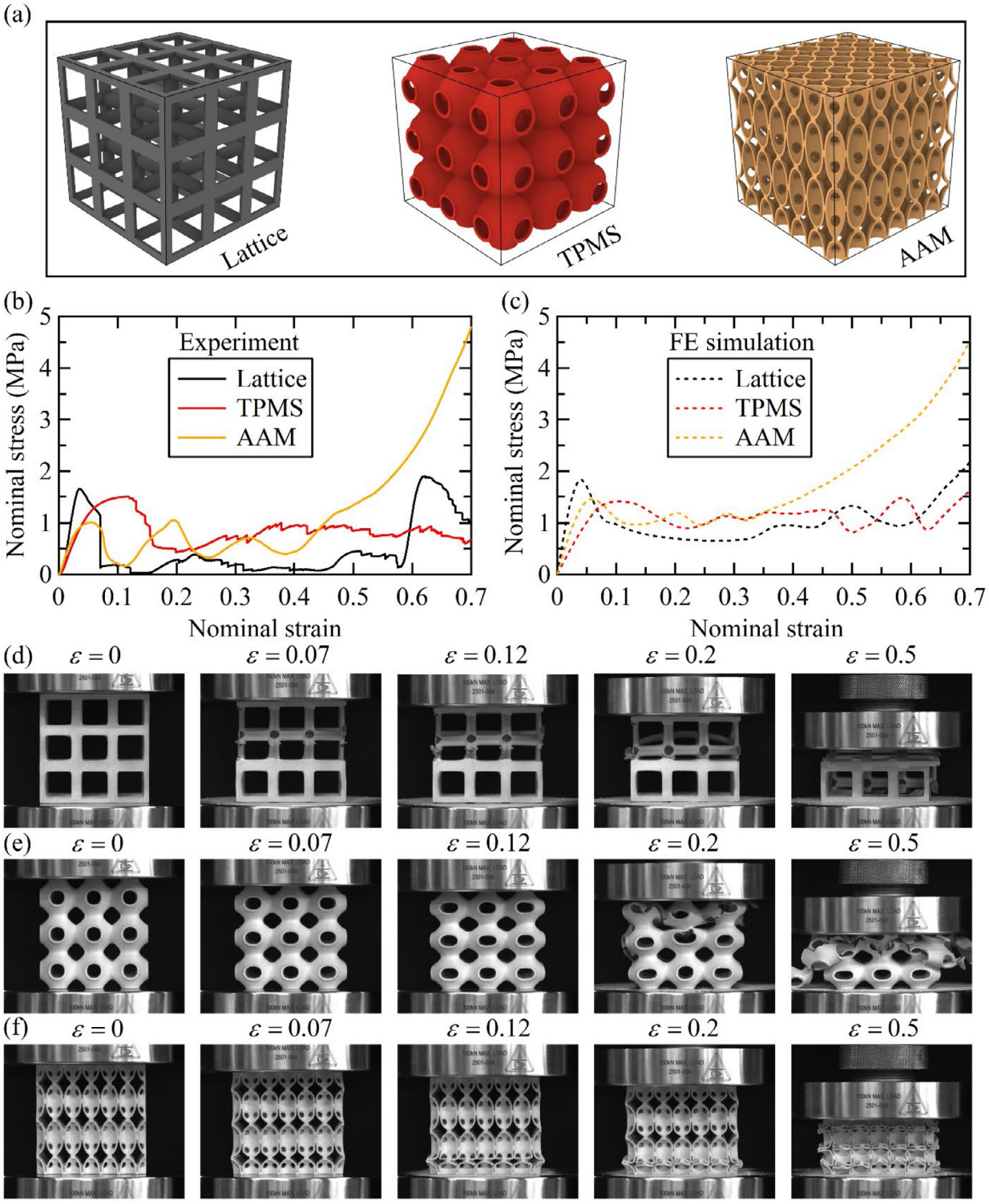

Fig. 6. Comparison of proposed AAM with existing lattices and TPMS model by experiment and simulation. (a) Geometrical model of SC-lattice, SC-TPMS, and AAM. (b) Experimental stress–strain relation of lattice, TPMS and AAM. (c) Simulated stress–strain relation of lattice, TPMS and AAM. (d)–(f) Deformation patterns of lattice, TPMS and AAM.

the stiffness and yield strength from FE simulations are very close to the experimental values. But the energy absorption of the three designs from simulations are quite different from the experimental values; this is due to the fact that in our simulations, we did not consider fracture and failure, which play a significant role in the mechanical behavior under large deformation; again, our simulation is not performed to match experimental results, and rather to provide insights to explain the deformation mechanism. Specifically, the stiffness of SC-lattice is much larger than that of SC-TPMS and AAM due to the strong stretch-dominated behavior when loading in [1] direction. Fig. 7**(c)** and **(d)** summarize the energy absorption of lattice, TPMS and AAM considering densification and without considering densification. It is observed that the energy absorption of AAM is better than the SC-lattice and SC-TPMS when densification is considered, as shown in Fig. 7**(c)**. However,

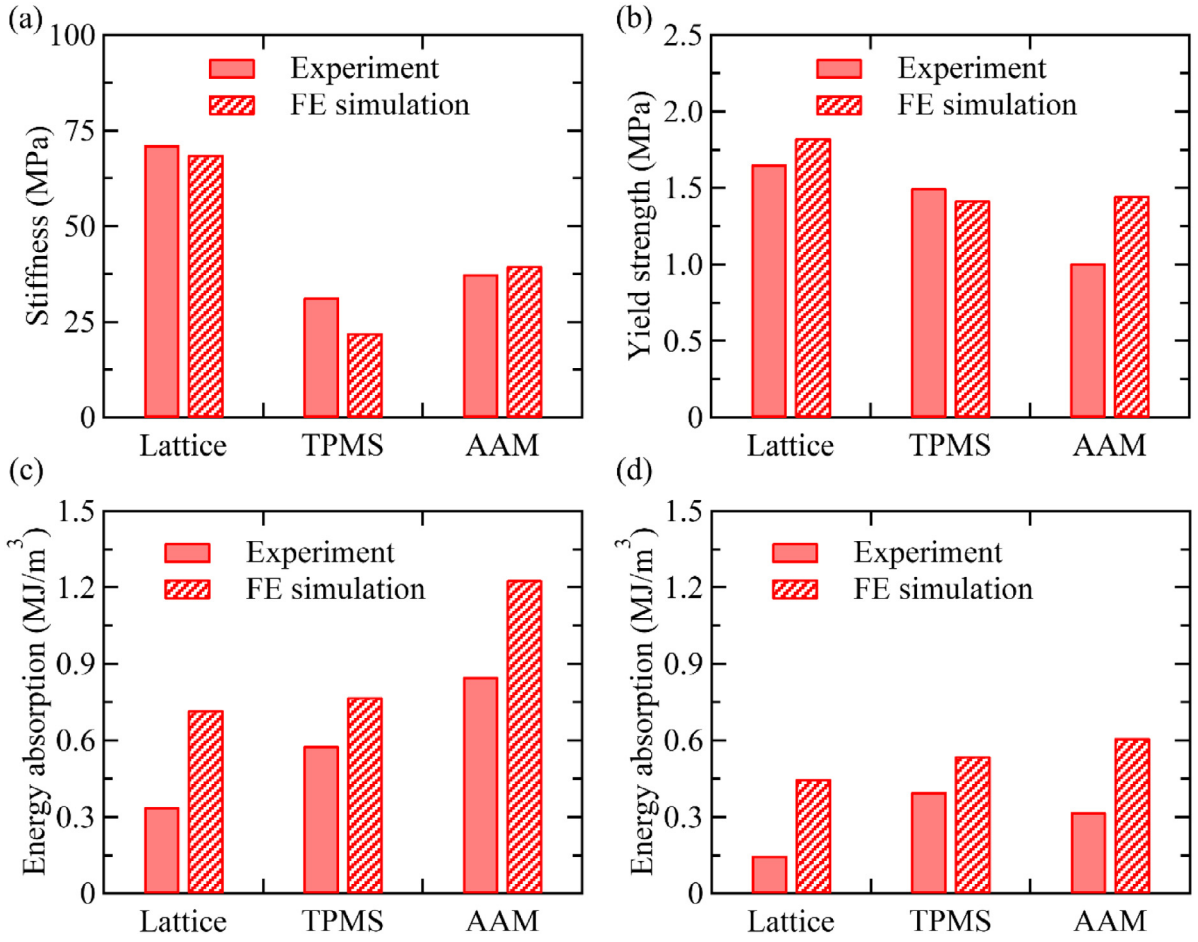

Fig. 7. Comparison of mechanical performance for lattice, TPMS and AAM. (a) Stiffness. (b) Yield strength. (c) Energy absorption considering densification. (d) Energy absorption before densification.

with respect to energy absorption efficiency (where densification is not considered), it is shown that our proposed AAM performs better than SC-lattice structure for both experiment and simulation; the energy absorption is increased by 120% and 35.6%, respectively. When comparing with SC-TPMS structure, the energy absorption of the proposed AAM from experiment is comparable to SC-TPMS. However, in the simulations without considering fractures, the energy absorption of AAM is increased by 13%. This suggests that fabricating AAM with more ductile material is preferred when energy absorption efficiency is considered.

The Mises stress contour plots for the AAM, SC-lattice, and SC-TPMS from FE simulation are shown in Fig. 8. At an applied strain of $\varepsilon = 0.07$, the stresses in the SC-lattice are mostly concentrated in the vertical beams at the top layer, leading to the significant buckling of these vertical beams. As the strain increases, a global buckling of the SC-lattice is observed, which causes the instability of the structure. This explains the significant stress drop in Fig. 6 (c) and the stress remains in the low range until densification. On the other hand, SC-TPMS is characterized by rather uniformly distributed stresses during the deformation. This has been extensively reported, and it is attributable to the smooth surface of TPMS with zero mean curvature [3,12]. As the applied strain is increased, however, the cells are significantly distorted, resulting in a layer-by-layer deformation pattern, which explains the peak–valley feature of stress–strain curve in the later stages of deformation as shown in Fig. 6**(c)**. In contrast, the AAM is characterized by the layer-by-layer buckling pattern throughout the simulation, as can be observed from the stress concentration on the different layers at different strains in Fig. 8**(c)**.

4. Conclusions

A new class of elastically anisotropic mechanical metamaterials has been developed that exhibit tunable anisotropy and enhanced energy absorption simply by altering the shape of the ellipsoidal shell that constitutes the microstructure. The proposed metamaterials with varying local architectures were manufactured via 3D printing. Through experimental tests and numerical simulations, we have investigated the effective elastic properties and the mechanical performance of these metamaterials under large deformation. From the scaling law relationship between relative density and relative stiffness, it was observed that as the ellipsoidal shell semi-major axis ratio of a/b increases, a more significant stretch-dominated behavior is expected. The anisotropy, as measured by the stiffness difference between the [100] and [001] directions in the metamaterials, can be tuned from 1-fold to 17-fold. By comparing the new metamaterials with existing SC-lattice and SC-TPMS microstructures, we report notable enhancement of energy absorption due to a stable layer-by-layer deformation pattern. Specifically, the energy absorption of the anisotropic metamaterials provided increases of 120% when compared to SC-lattice. Meanwhile, the energy absorption of anisotropic metamaterials is comparable to SC-TPMS structure. The findings presented in this work demonstrate the utility of AAMs for applications where good energy absorption and anisotropy are both required, such as bone scaffolding and battery separators. For example, the stiffness and energy absorption of the cancellous bone are largely affected by the trabeculae in the longitudinal direction; in contrast, the mechanical significance of trabeculae in the transverse direction is only served as the purpose to endure off-axis loading [55,56]. This requires that the bone scaffolds show significant mechanical performance in

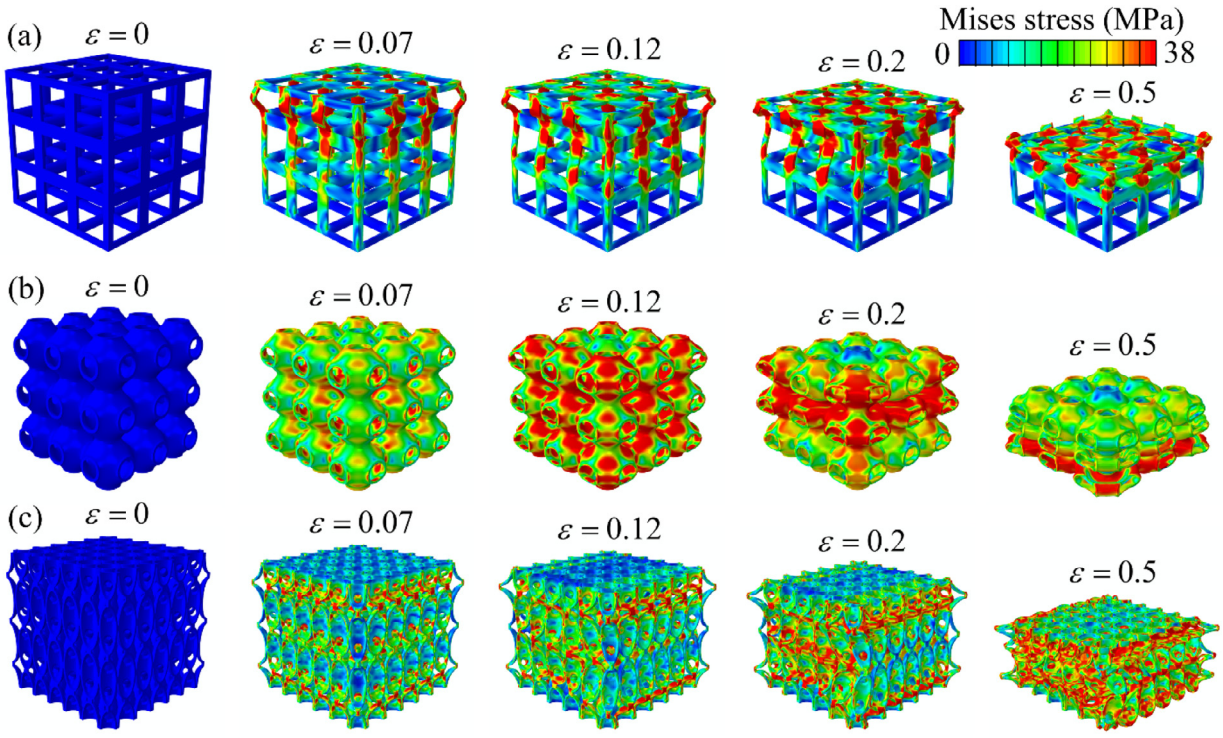

Fig. 8. Von Mises contour plots of lattice, TPMS and AAM. (a) Mises contour plots of lattice. (b) Mises contour plots of TPMS. (c) Mises contour plots of AAM.

the longitudinal direction while far less performance is needed in the transverse direction. The stiffness of battery separators along the machine direction has been reported to be notably larger than the transverse direction [23]. Meanwhile, efficient energy absorption is necessary for lithium-ion battery separators when subject to mechanical abuse during operation.

CRediT authorship contribution statement

Huan Jiang: Writing – original draft, Visualization, Methodology, Investigation, Formal analysis. **Brett A. Bednarcyk:** Writing – review & editing, Resources, Methodology, Investigation, Formal analysis. **Louise Le Barbenchon:** Writing – review & editing, Resources, Methodology, Investigation, Formal analysis. **Yanyu Chen:** Writing – review & editing, Writing – original draft, Supervision, Resources, Project administration, Investigation, Funding acquisition, Formal analysis, Conceptualization.

Declaration of competing interest

The authors declare that they have no known competing financial interests or personal relationships that could have appeared to influence the work reported in this paper.

Data availability

Data will be made available on request.

Acknowledgments

Y. Chen gratefully acknowledges the financial support of the National Science Foundation, USA, CMMI Mechanics of Materials and Structures Program, USA (Award Number: 2114823) and Office of Integrative Activities, USA (Award Number: 2226563).

Appendix A. Supplementary data

Supplementary material related to this article can be found online at https://doi.org/10.1016/j.tws.2023.111115.

References

[1] X. Zheng, H. Lee, T.H. Weisgraber, M. Shusteff, J. DeOtte, E.B. Duoss, J.D. Kuntz, M.M. Biener, Q. Ge, J.A. Jackson, S.O. Kucheyev, N.X. Fang, C.M. Spadaccini, Ultralight, ultrastiff mechanical metamaterials, Science 344 (6190) (2014) 1373–1377.
[2] C. Crook, J. Bauer, A. Guell Izard, C. Santos de Oliveira, J. Martins de Souza e Silva, J.B. Berger, L. Valdevit, Plate-nanolattices at the theoretical limit of stiffness and strength, Nature Commun. 11 (1) (2020) 1579.
[3] S.C. Han, K. Kang, Another stretching-dominated micro-architectured material, shellular, Mater. Today 31 (2019) 31–38.
[4] S. Shan, S.H. Kang, J.R. Raney, P. Wang, L. Fang, F. Candido, J.A. Lewis, K. Bertoldi, Multistable architected materials for trapping elastic strain energy, Adv. Mater. 27 (29) (2015) 4296–4301.
[5] R. Hamzehei, A. Zolfagharian, S. Dariushi, M. Bodaghi, 3D-printed bio-inspired zero Poisson's ratio graded metamaterials with high energy absorption performance, Smart Mater. Struct. 31 (3) (2022) 035001.
[6] R. Hamzehei, A. Serjouei, N. Wu, A. Zolfagharian, M. Bodaghi, 4D metamaterials with zero Poisson's ratio, shape recovery, and energy absorption features, Adv. Eng. Mater. 24 (9) (2022) 2200656.
[7] X.H. Ni, W. Jiang, X.G. Zhang, D. Han, X.C. Teng, J. Hao, H.H. Xu, X. Ren, Quasi-static and dynamic properties studies of a metamaterial with enhanced auxeticity and tunable stiffness, Compos. Struct. 321 (2023) 117254.
[8] D. Han, Y. Zhang, X.Y. Zhang, Y.M. Xie, X. Ren, Lightweight auxetic tubular metamaterials: Design and mechanical characteristics, Compos. Struct. 311 (2023) 116849.
[9] S.-Y. Jeon, B. Shen, N.A. Traugutt, Z. Zhu, L. Fang, C.M. Yakacki, T.D. Nguyen, S.H. Kang, Synergistic energy absorption mechanisms of architected liquid crystal elastomers, Adv. Mater. 34 (14) (2022) 2200272.
[10] M.C. Fernandes, J. Aizenberg, J.C. Weaver, K. Bertoldi, Mechanically robust lattices inspired by deep-sea glass sponges, Nature Mater. 20 (2) (2021) 237–241.
[11] W. Huang, M. Shishehbor, N. Guarín-Zapata, N.D. Kirchhofer, J. Li, L. Cruz, T. Wang, S. Bhowmick, D. Stauffer, P. Manimunda, K.N. Bozhilov, R. Caldwell, P. Zavattieri, D. Kisailus, A natural impact-resistant bicontinuous composite nanoparticle coating, Nature Mater. 19 (11) (2020) 1236–1243.
[12] H. Jiang, L. Le Barbenchon, B.A. Bednarcyk, F. Scarpa, Y. Chen, Bioinspired multilayered cellular composites with enhanced energy absorption and shape recovery, Addit. Manuf. 36 (2020) 101430.

[13] A.M. Torres, A.A. Trikanad, C.A. Aubin, F.M. Lambers, M. Luna, C.M. Rimnac, P. Zavattieri, C.J. Hernandez, Bone-inspired microarchitectures achieve enhanced fatigue life, Proc. Natl. Acad. Sci. 116 (49) (2019) 24457–24462.
[14] Z. Liu, Z. Zhang, R.O. Ritchie, Structural orientation and anisotropy in biological materials: Functional designs and mechanics, Adv. Funct. Mater. 30 (10) (2020) 1908121.
[15] C. Chen, Y. Kuang, S. Zhu, I. Burgert, T. Keplinger, A. Gong, T. Li, L. Berglund, S.J. Eichhorn, L. Hu, Structure–property–function relationships of natural and engineered wood, Nat. Rev. Mater. 5 (9) (2020) 642–666.
[16] X. Wang, J. Fang, W. Zhu, C. Zhong, D. Ye, M. Zhu, X. Lu, Y. Zhao, F. Ren, Bioinspired highly anisotropic, ultrastrong and stiff, and osteoconductive mineralized wood hydrogel composites for bone repair, Adv. Funct. Mater. 31 (20) (2021) 2010068.
[17] J. Kang, E. Dong, D. Li, S. Dong, C. Zhang, L. Wang, Anisotropy characteristics of microstructures for bone substitutes and porous implants with application of additive manufacturing in orthopaedic, Mater. Des. 191 (2020) 108608.
[18] G.Y. Gor, J. Cannarella, J.H. Prévost, C.B. Arnold, A model for the behavior of battery separators in compression at different strain/charge rates, J. Electrochem. Soc. 161 (11) (2014) F3065–F3071.
[19] X. Zhang, E. Sahraei, K. Wang, Deformation and failure characteristics of four types of lithium-ion battery separators, J. Power Sources 327 (2016) 693–701.
[20] J. Zhu, T. Wierzbicki, W. Li, A review of safety-focused mechanical modeling of commercial lithium-ion batteries, J. Power Sources 378 (2018) 153–168.
[21] B. Liu, Y. Jia, C. Yuan, L. Wang, X. Gao, S. Yin, J. Xu, Safety issues and mechanisms of lithium-ion battery cell upon mechanical abusive loading: A review, Energy Storage Mater. 24 (2020) 85–112.
[22] C. Yuan, L. Wang, S. Yin, J. Xu, Generalized separator failure criteria for internal short circuit of lithium-ion battery, J. Power Sources 467 (2020) 228360.
[23] J. Xu, L. Wang, J. Guan, S. Yin, Coupled effect of strain rate and solvent on dynamic mechanical behaviors of separators in lithium ion batteries, Mater. Des. 95 (2016) 319–328.
[24] C.F.J. Francis, I.L. Kyratzis, A.S. Best, Lithium-ion battery separators for ionic-liquid electrolytes: A review, Adv. Mater. 32 (18) (2020) 1904205.
[25] C.M. Portela, A. Vidyasagar, S. Krödel, T. Weissenbach, D.W. Yee, J.R. Greer, D.M. Kochmann, Extreme mechanical resilience of self-assembled nanolabyrinthine materials, Proc. Natl. Acad. Sci. 117 (11) (2020) 5686–5693.
[26] S. Kumar, S. Tan, L. Zheng, D.M. Kochmann, Inverse-designed spinodoid metamaterials, npj Comput. Mater. 6 (1) (2020) 73.
[27] F.V. Senhora, E.D. Sanders, G.H. Paulino, Optimally-tailored spinodal architected materials for multiscale design and manufacturing, Adv. Mater. 34 (26) (2022) 2109304.
[28] J.B. Berger, H.N.G. Wadley, R.M. McMeeking, Mechanical metamaterials at the theoretical limit of isotropic elastic stiffness, Nature 543 (7646) (2017) 533–537.
[29] H. Jiang, A. Coomes, Z. Zhang, H. Ziegler, Y. Chen, Tailoring 3D printed graded architected polymer foams for enhanced energy absorption, Composites B 224 (2021) 109183.
[30] O. McGee, H. Jiang, F. Qian, Z. Jia, L. Wang, H. Meng, D. Chronopoulos, Y. Chen, L. Zuo, 3D printed architected hollow sphere foams with low-frequency phononic band gaps, Addit. Manuf. 30 (2019) 100842.
[31] H. Jiang, Y. Chen, Lightweight architected hollow sphere foams for simultaneous noise and vibration control, J. Phys. D: Appl. Phys. 52 (32) (2019) 325303.
[32] M.I.J.M. Kohan, Nylon Plastics Handbook, Hanser, 1995.
[33] R. Hamzehei, M. Bodaghi, J.A. Iglesias Martinez, Q. Ji, G. Ulliac, M. Kadic, C. Wang, A. Zolfagharian, N. Wu, Parrot beak-inspired metamaterials with friction and interlocking mechanisms 3D/4D printed in micro and macro scales for supreme energy absorption/dissipation, Adv. Eng. Mater. 25 (11) (2023) 2201842.
[34] A. Yousefi, S. Jolaiy, M. Lalegani Dezaki, A. Zolfagharian, A. Serjouei, M. Bodaghi, 3D-printed soft and hard meta-structures with supreme energy absorption and dissipation capacities in cyclic loading conditions, Adv. Eng. Mater. 25 (4) (2023) 2201189.
[35] R. Tahzeeb, M. Alam, S.M. Muddassir, A comparative performance of columns: reinforced concrete, composite, and composite with partial C-FRP wrapping under contact blast, Mater. Today: Proc. 62 (2022) 2191–2202.
[36] R. He, L.G. Zhao, V.V. Silberschmidt, Y. Liu, F. Vogt, Finite element evaluation of artery damage in deployment of polymeric stent with pre- and post-dilation, Biomech. Model. Mechanobiol. 19 (1) (2020) 47–60.
[37] F. Taheri-Behrooz, E. Pourahmadi, A 3D RVE model with periodic boundary conditions to estimate mechanical properties of composites, Struct. Eng. Mech. 72 (6) (2019) 713–722.
[38] P. Suquet, Elements of homogenization theory for inelastic solid mechanics, in: E. Sanchez-Palencia, A. Zaoui (Eds.), Homogenization Techniques for Composite Media, Springer-Verlag, Berlin, 1987.
[39] Z. Xia, C. Zhou, Q. Yong, X. Wang, On selection of repeated unit cell model and application of unified periodic boundary conditions in micro-mechanical analysis of composites, Int. J. Solids Struct. 43 (2) (2006) 266–278.
[40] X. Tan, S. Chen, B. Wang, J. Tang, L. Wang, S. Zhu, K. Yao, P. Xu, Real-time tunable negative stiffness mechanical metamaterial, Extreme Mech. Lett. 41 (2020) 100990.
[41] H. Jiang, H. Ziegler, Z. Zhang, H. Meng, D. Chronopoulos, Y. Chen, Mechanical properties of 3D printed architected polymer foams under large deformation, Mater. Des. 194 (2020) 108946.
[42] Y. Duan, B. Du, X. Shi, B. Hou, Y. Li, Quasi-static and dynamic compressive properties and deformation mechanisms of 3D printed polymeric cellular structures with Kelvin cells, Int. J. Impact Eng. 132 (2019) 103303.
[43] A. Hössinger-Kalteis, M. Reiter, M. Jerabek, Z. Major, Overview and comparison of modelling methods for foams, J. Cellular Plastics 57 (6) (2021) 951–1001.
[44] M.F. Ashby, The properties of foams and lattices, Phil. Trans. R. Soc. A 364 (1838) (2006) 15–30.
[45] S.C. Han, K.J.M.T. Kang, Another stretching-dominated micro-architectured material, shellular, 31, 2019, pp. 31–38.
[46] S.C. Han, J.W. Lee, K.J.A.M. Kang, A new type of low density material: Shellular, 27, (37) 2015, pp. 5506–5511.
[47] F. Chen, Y. Miao, L. Zhang, S. Chen, X. Zhu, Triply periodic channels enable soft pneumatic linear actuator with single material and scalability, IEEE Robot. Autom. Lett. 7 (2) (2022) 2668–2675.
[48] H.S. Abdulhadi, A. Fadeel, T.A. Alwattar, A. Mian, Developing scaling laws to predict compressive mechanical properties and determine geometrical parameters of modified BCC lattice structures, Eng. Rep. (2022) e12566.
[49] K. Krishnan, D.-W. Lee, M. Al Teneji, R.K. Abu Al-Rub, Effective stiffness, strength, buckling and anisotropy of foams based on nine unique triple periodic minimal surfaces, Int. J. Solids Struct. 238 (2022) 111418.
[50] T. Tancogne-Dejean, M. Diamantopoulou, M.B. Gorji, C. Bonatti, D. Mohr, 3D plate-lattices: An emerging class of low-density metamaterial exhibiting optimal isotropic stiffness, Adv. Mater. 30 (45) (2018) 1803334.
[51] M. Munford, U. Hossain, S. Ghouse, J.R.T. Jeffers, Prediction of anisotropic mechanical properties for lattice structures, Addit. Manuf. 32 (2020) 101041.
[52] J. Nordmann, M. Azmus, H. Altenbach, Visualising elastic anisotropy: theoretical background and computational implementation, Contin. Mech. Thermodyn. 30 (4) (2018) 689–708.
[53] T. Tancogne-Dejean, D. Mohr, Stiffness and specific energy absorption of additively-manufactured metallic BCC metamaterials composed of tapered beams, Int. J. Mech. Sci. 141 (2018) 101–116.
[54] T. Tancogne-Dejean, D. Mohr, Elastically-isotropic elementary cubic lattices composed of tailored hollow beams, Extreme Mech. Lett. 22 (2018) 13–18.
[55] T.E. Ciarelli, D.P. Fyhrie, M.B. Schaffler, S.A. Goldstein, Variations in three-dimensional cancellous bone architecture of the proximal femur in female hip fractures and in controls, J. Bone Miner. Res.: Off. J. Am. Soc. Bone Miner. Res. 15 (1) (2000) 32–40.
[56] J. Homminga, B. Van-Rietbergen, E.M. Lochmüller, H. Weinans, F. Eckstein, R. Huiskes, The osteoporotic vertebral structure is well adapted to the loads of daily life, but not to infrequent error loads, Bone 34 (3) (2004) 510–516.